Atomic resolution imaging of the strength and 3D direction of atomic displacements in functional oxide thin films

Ian Maclaren,[1,*] Aurys Silinga,[1] Juri Barthel,[2] Josee Kleibeuker,[3,4] Judith L MacManus-Driscoll,[3] Christopher S. Allen,[5,6] and Angus I. Kirkland[5,6]

[1]*School of Physics and Astronomy, University of Glasgow, Glasgow G12 8QQ, United Kingdom*
[2]*Ernst Ruska-Centre (ER-C 2), Forschungszentrum Jülich GmbH, 52425 Jülich, Germany*
[3]*Department of Materials Science and Metallurgy, University of Cambridge, 27 Charles Babbage Road, Cambridge CB3 OFS, United Kingdom*
[4]*DEMCON high tech systems Eindhoven BV, Kanaaldijk 29, 5683 CR Best, The Netherlands*
[5]*electron Physical Science Imaging Centre, Diamond Light Source Ltd., Didcot OX11 0DE, United Kingdom*
[6]*Department of Materials, University of Oxford, Parks Road, Oxford OX1 3PH, United Kingdom*

(Received 25 March 2025; revised 9 July 2025; accepted 21 August 2025; published 4 September 2025)

Atomic resolution imaging is key to understanding thin film growth and how a particular set of conditions influences properties. Whilst such imaging in the scanning transmission electron microscope (STEM) has had a transformative impact in nanoscience, it forms projection images and provides no direct information about displacements perpendicular to the image plane. In this article, we show that it is possible to make atomic resolution maps of the direction and magnitude of La displacements at ~30° to the imaging plane in a La_2CoMnO_6 thin film on (111) LSAT ($LaAlO_3$−$La(Sr, Ta)O_3$) using a four-dimensional STEM (4DSTEM) methodology. This reveals that the La modulation lies preferentially in the interface plane, and is strongly suppressed close to the epitaxial interface, and further reveals how the modulation varies with distance from the interface with unit cell resolution. These details would be completely invisible to all prior techniques in electron microscopy and this sheds light on why this particular substrate in this orientation best promotes double perovskite cation ordering, and the consequent optimal magnetic ordering for this thin film system. The approach used herein of fitting atomic resolution 4DSTEM data to determine crystal parameters opens the door for a new era of atomic-resolution crystallography.

DOI: 10.1103/p6qm-hpvk

I. INTRODUCTION

Atomic resolution imaging in the scanning transmission electron microscope (STEM) has revolutionised science and technology, especially since the introduction of aberration correction [1,2], making sub-Ångström resolution easily realized. The ability to simply see two-dimensional projections of the atomic structure in thin specimens of crystalline solids has allowed unprecedented understanding of local features in nanostructures, such as interfaces, as well as of defects within materials and heterostructures [3–5]. In specific cases, more information about the three-dimensional structure can be determined by looking at multiple examples of the same structure using discrete tomography [6–8], or from conventional tilt-tomography, although the latter is hard to perform at atomic resolution [9] at reasonable fluence levels. Recently, however, major advances have been made in STEM with the advent of fast-readout direct electron detectors for 4DSTEM (four-dimensional scanning transmission electron microscopy) [10,11], which offers possibilities for novel imaging modalities not possible with monolithic annular [12–14], circular [15] or segmented detectors [16,17]. We have previously shown that high-angle electron diffraction into higher-order Laue zones produces an atomic resolution signal [18], which reveals information about the 3D order in a crystal. This current work goes far beyond that and shows that the atomic resolution diffraction data contains information about the exact 3D orientation of one unique axis of the unit cell and the magnitudes of atom movements along it; and that this can be mapped at atomic resolution by fitting a simple mathematical model. In short, we show that by measuring and fitting high-angle scattering, 4DSTEM can perform atomic resolution imaging of 3D crystal ordering without any need for sample tilting. Such approaches will provide a major step forward in understanding the details of nanoscale heterostructures, including surface reconstructions and interface structures.

Characterizing the local crystallographic structure of materials is key to understanding their behavior and how the growth or fabrication leads to a given structure with specific properties. However, despite the ability of electron microscopy to image nanostructures with atomic resolution,

*Contact author: ian.maclaren@glasgow.ac.uk

Published by the American Physical Society under the terms of the Creative Commons Attribution 4.0 International license. Further distribution of this work must maintain attribution to the author(s) and the published article's title, journal citation, and DOI.

this remains a two-dimensional projection, and gaining access to information in the third dimension is very challenging in dimensionally constrained samples such as few-nm thin films or domain structures. Such considerations are especially pertinent when considering the optimization of functional oxides and other functional materials, which are often grown as epitaxial systems with interfaces exerting a significant control over the resulting structure, chemical ordering and properties, particularly through strain transfer. However, we previously demonstrated that some information about the periodicity in the third dimension was available using a *HOLZ-STEM* (higher-order Laue zone – scanning transmission electron microscopy) approach [19], and that this is atomically resolved [18] (as also shown without 4DSTEM by Huang *et al.* [20]). This only recently became convenient to perform because of the advent of 4DSTEM, in which a scan is performed over an area with a diffraction pattern recorded to a suitably fast detector at every scan point [10,11]. Nevertheless, more directional information than this about atomic displacements was absent until now.

A common feature of functional oxides is octahedral coordination of the smaller cations and the coordinated tilting of these octahedra, often coupled with antiparallel displacements of the larger cations [21]. Whilst octahedral tilting is particularly common in perovskites and there exists a specific classification scheme for the tilting patterns thereof [22], similar effects are observed in a much wider range of functional oxides. This is particularly likely where the unit cell contains more than one similar layer and the cation is located away from a centrosymmetric position, as is seen, for example, in some tungsten bronzes [23]. This work particularly focuses on La_2CoMnO_6 (LCMO), which can order as a double perovskite with the B-site Co and Mn forming charge order as Co^{2+} and Mn^{4+} and ordering on two interpenetrating face-centered lattices in a monoclinic cell ($P2_1/n$) with $a = 5.52464$ Å, $b = 5.48302$ Å, $c = 7.7717$ Å, $\beta = 89.898°$ (as refined by Bull *et al.* [24]). Figure 1 shows a side view of a one-atom-thick slice of the structure of LCMO, (although with displacements exaggerated to make them clearer to the reader), showing such antiparallel displacements of alternate La atoms along the [111] direction (vertical in the figure), the displacements from equally spaced positions when viewed along a $\langle 111\rangle_M$ or $\langle 11\bar{1}\rangle_M$ direction being parallel to the **b** direction (actually $\mathbf{d} = \pm 0.0216[010]_M$, c.f. Supplemental Material [25] Sec. S1 for derivation). A key point is that rotating the crystal by 180° about the beam direction ($[111]_M$ in the figure) does not result in equivalent 3D structures, one showing an up-left, down-right pattern, and the other an up-right, down-left pattern. Despite this clear difference in 3D structure, projection images of any sort (such as annular dark field STEM) taken along $[111]_M$ from crystals represented by the two panes of Fig. 1 would be identical. A 3D view of these coordinated atom movements and how they relate to the sample overall (e.g., at interfaces and strain fields) would be invaluable in better understanding the growth of complex oxides, especially in the presence of interfaces and/or multiple domains on the nanoscale. Either of these would make tilt tomography approaches impracticable. This would in turn inform the optimization of the growth to produce atomic structures with the desired properties. The present work shows that using a 4DSTEM/HOLZ-STEM approach, it is possible to determine these out-of-plane displacements at atomic resolution and use those to map out the displacement patterns close to an epitaxial interface.

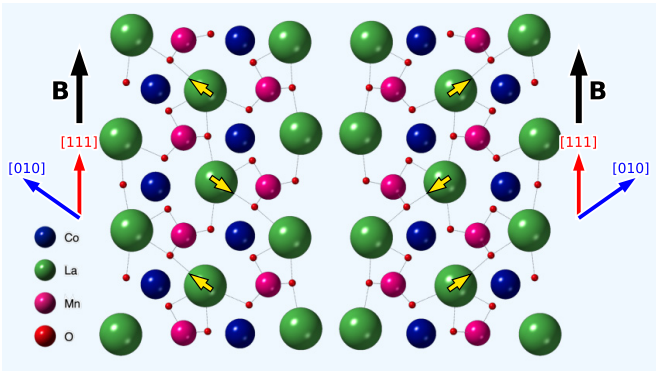


FIG. 1. Schematic view of columns of atoms along the $[111]_M$ direction (vertical) in La_2CoMnO_6, in which there are alternate antiparallel La cation displacements along a direction parallel to $[010]_M$. Two possible orientations of the crystal are shown, containing the same vertical $[111]_M$ direction, but differing by a 180° rotation about the vertical direction). These two crystal orientations would give indistinguishable projection images when recorded with a beam direction parallel to $[111]_M$ (i.e., the 2D projection symmetry includes a twofold rotation), however, the 3D orientation of the ***b***-axis is switched. Just one plane of the crystal is shown for simplicity. La atom displacements are magnified by a factor of 3 to aid visualization.

II. METHODS

A. Sample preparation and scanning transmission electron microscopy

The LCMO sample was grown by pulsed laser deposition on a (111) substrate of LSAT ($LaAlO_3$−(La, Sr)TaO_3) at a substrate temperature of 710 °C using a repetition rate of 1Hz and a fluence of 1.5J cm^{-2} under 0.15 mbar flowing O_2, followed by annealing at 700 °C for 30 min under 500 mbar O_2, and finally slow cooling to room temperature. A sample was prepared for STEM using a standard FIB liftout procedure. Further details are given in Kleibeuker *et al.* [26].

Scanning transmission electron microscope datasets were acquired using a JEOL ARM300F at the ePSIC facility at Diamond Light Source, operated at 200 kV, with the diffraction patterns acquired using a 2 × 2 tiled Medipix detector providing 515 × 515 pixel images (Quantum Detectors Ltd., UK). The convergence angle of the probe was 20 mrad, and the camera length was set to allow angles of up to about 97 mrad to reach the detector (center to middle of edge), and a step size of ∼ 0.5 Å was used to collect the dataset shown. The microscope defocus was tuned to give the best atomic-resolution HAADF imaging since this should give the best resolution of diffraction information in 4DSTEM, and defocus can be considered to be close to 0 nm or very slightly underfocused (i.e., focused at the top of the sample). No attempts were made to vary defocus or examine the effects of doing so experimentally, although simulations were performed on the effects thereof, and these are in the Supplemental Material [25],

Sec. S4. In summary, the main features in the parameter maps shown below are shown as long as good atomic-resolution HAADF images are produced.

B. Data handling and initial processing (polar transform and fitting)

Conversion of the raw data to HDF5 was performed on site at Diamond Light Source, and all calculations were done on datasets where the diffraction dimension had been binned by a factor of 4 prior to further processing, since this both reduced memory requirements and increased processing speed, with no noticeable loss of any information in the results of the analysis. The center of the FOLZ ring in the dataset was determined by overlaying a circle on the data and shifting this until it best matched the ring (as the center-of-mass of the diffraction pattern, dominated by low-angle scattering, can differ slightly from the center of the FOLZ, if there is slight sample mistilt). This was then followed by performing the polar transform and testing if the Laue zone ring is a straight line after the transform.

Polar transform over entire 4DSTEM datasets was performed using home-built code (provided in the data deposit, alongside all other code pieces and raw data used in this work) based on the earlier implementation of Barthel in *emilys*, using the same maths, but optimized for fast calculation of an entire dataset. The relevant feature of the FOLZ ring was identified (the outer part of the split ring [18]) corresponding most strongly to the La-O columns and integrated into a 1D line plot of intensity as a function of azimuthal angle.

This was then fitted to Eq. (1):

$$I(\phi) = A_2\cos^2(\phi - \phi_2) + A_1\cos(\phi - \phi_1) + B, \qquad (1)$$

(which is the fit function described in our previous, although some parameter renaming has been performed to aid clarity of understanding the meaning of each parameter from its name). A_2 is the amplitude of the twofold intensity modulation, ϕ_2 is the peak angle of that twofold modulation (defined in the range of 0 to 180°), A_1 is the amplitude of the onefold intensity modulation, ϕ_1 is the angular shift of that onefold modulation (defined in the range of 0 to 360°), and B is the offset from zero. Fitting to the function was performed using *scipy.optimize.curve_fit* using a simple iterative function that fits each pixel in the real space scan in turn.

C. A note on structures and notation

LSAT is pseudocubic (notwithstanding nanoscale chemical and likely structural variations), and directions and planes referenced to a primitive cubic perovskite cell have the subscript C, e.g., $(111)_C$.

LCMO, as noted above, is monoclinic with a, b, $c \approx \sqrt{2}a_C, \sqrt{2}a_C, 2a_C$. Directions and planes referenced to this cell have a subscript M, e.g., $[111]_M$. The A-site modulation is close to $[010]_M$. "***b***-axis" only ever refers to the M structure.

Some of the related structures discussed in the discussion have orthorhombic structures, which can either be expressed as *Pbnm* or *Pnma*, two alternate settings of space group 62. *Pbnm* is the easier of the two to relate to the monoclinic cell, as the axes come in exactly the same order with similar relative lengths. *Pnma* is also used, with the A-site modulation close to $[100]_{Pnma}$. Either *Pnma* or *Pbnm* is used as the subscript in these cases.

D. Multislice simulation of 4DSTEM datasets and matching to experiment

Simulated 4DSTEM datasets were calculated from the structure of Bull *et al.* [24] using a multislice approach with the Dr. Probe package [27], for a sample thickness of 53 nm. For the multislice simulations of the structure in $[111]_M$ orientation, a supercell of size $a_{SC} = 3.84731$ nm, $b_{SC} = 3.89183$ nm, & $c_{SC} = 1.10062$ nm and orthogonalized unit vectors was set up and partitioned into eight slices along the $\mathbf{c}_{SC}$ direction, i.e., the direction parallel to that of the incident electron probe. The slices were set such that each contains one atomic plane. Projected scattering potentials were prepared on a grid of 800×864 pixels for the $(\mathbf{a}_{SC}, \mathbf{b}_{SC})$ planes. For simulating the effects of thermal diffuse scattering within the quantum excitation of phonons (QEP) model [28], 100 atomic configurations were prepared for each slice. High-angle diffraction patterns were calculated for a pixelated detector of 384×384 pixels placed in the diffraction plane (far field) with a pixel step of 0.25 mrad, assuming the experimental STEM parameters noted above, and for every point in a scan at a similar pixel sampling to the experimental data. This simulated 4DSTEM dataset was processed in the same way as the experimental data, and when comparing to experimental datasets averaged from many unit cells, it should be noted that the theoretical simulation is also the average of 100 different QEP simulations.

The experimental dataset for comparison was interpolated by a factor of 4 using *scipy.ndimage.zoom,* and then 121 unit cell origins were found on La-O columns using *Atomap* [29] and used to determine image patches for superposition and summation—the interpolation meant that the results were not smeared by the origin positions varying at the subpixel level.

E. Mapping of the displacements in 3D

To convert a map of fit parameters to a map of ***b***-axis orientations first needs sets of peak positions to be determined with *Atomap* [29]: La-column HAADF peaks and the peak positions in the A_1 map (being easier to quantify reliably than the trough positions). These are then sorted by coordinates and nearest-neighbor A_1-site peaks are associated with each La column peak (i.e., HAADF peak) in sorted lists. These are then used to give the sense of the ***b***-axis in 3D (not just projected into 2D). The angles are determined from the average of a patch around each HAADF peak (3×3 in this work, but this would be easy to adjust to 5×5 if desired). The strength of the La position modulation is determined from the A_2 values at the peaks of A_1 (the troughs are more difficult to find reliably). The resulting data can then be plotted as a map of the **d** orientation, and modulation strength (atom off-center shift), normalized to the maximum value observed previously by structure refinement [24]. This plot can then be displayed using a range of representations (e.g., arrow or "quiver" plot, colormap). Note, whilst we expect the **d**-direction to be

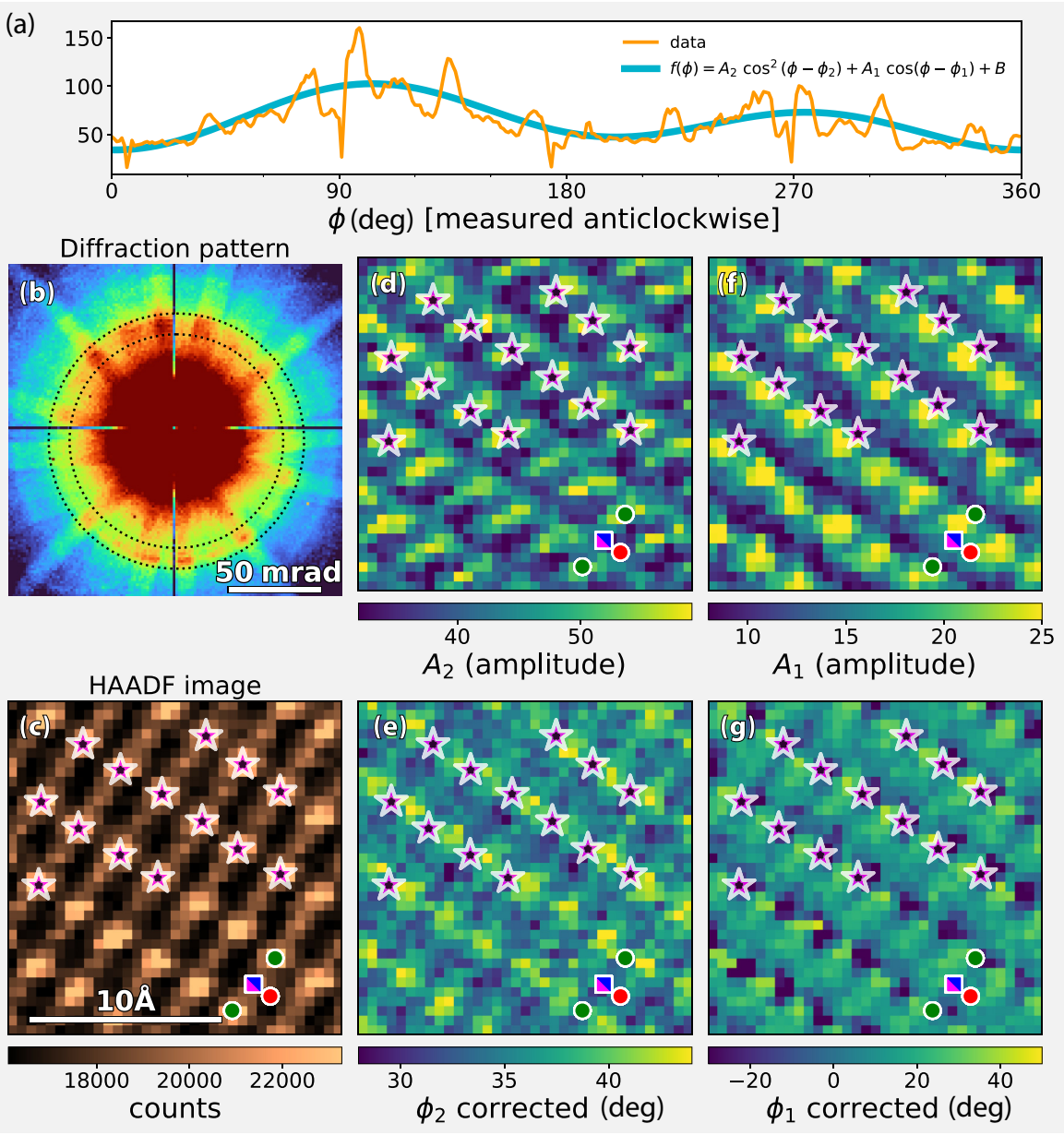


FIG. 2. Atomic resolution fitting of the first-order Laue zone ring in a region of a La_2CoMnO_6 film calculated from a 4DSTEM dataset recorded along a $\langle 111 \rangle_M$ direction. This shows (b) a sum diffraction pattern from the whole area with the FOLZ ring indicated with dotted lines; (a) the fit of the ring from this sum pattern after polar transformation; (c) a HAADF image calculated from the dataset for angles > 79 mrad; and (d)–(g) fit maps for the parameters A_2, ϕ_2, A_1, and ϕ_1 as defined in Eq. (1) and the legend of part (b). An overlay of La-O atomic column positions is given on maps (c)–(g), together with a unit cell key (green–La-O, magenta/blue–manganese/cobalt, red–O).

parallel to **b**, it is plausible that it could deviate from such a crystallographic alignment locally, especially close to boundaries or defects, so the orientation is worth mapping at high resolution.

III. RESULTS

A. Fitting the azimuthal diffracted intensity variation at atomic resolution

We showed recently that unidirectional atom position modulations, as shown in Fig. 1, lead to a strong periodic azimuthal intensity variation in the first-order Laue zone (FOLZ) ring clearly aligned with the modulation direction. It was shown that this can be used to determine the modulation direction and strength through fitting the azimuthal variation to a simple periodic function [30], in a way that is far more accurate and informative than simple atomic resolution imaging. However, this was just performed on larger image patches covering several unit cells, and no attempt was made to do so at atomic resolution, or to investigate the details of what might emerge from such fitting at atomic resolution. Figure 2(b) shows a representative diffraction pattern averaged over a significant image area (to improve signal-to-noise) with the FOLZ indicated within dotted lines describing two concentric circles. The data was polar transformed and then integrated into a single intensity plot as a function of azimuthal angle

(measured counterclockwise from horizontal-right) for fitting to Eq. (1). The fit shown in Fig. 2(a) clearly peaks close to 90° and 270°, with additional intensity on the 90° side (top of diffraction pattern). The remainder of Fig. 2 shows the results of applying this approach to every pixel of an atomic resolution 4DSTEM scan of a single crystal area of a La_2CoMnO_6 thin film (grown on $LaAlO_3$−(Sr, Ta)AlO_3−LSAT) [26]. A HAADF image was calculated from the polar-transformed data by simply integrating all intensity above a scattering angle of 79 mrad, and this shows the expected appearance for a perovskite viewed along a $\langle 110\rangle_C$ direction. The centers of the brightest peaks in the upper half of the image (as determined using Gaussian interpolation), arising from La-O columns, are indicated by fuchsia stars, and these stars are overlaid on the equivalent images from the FOLZ fitting. Figures 2(d)–2(g) show the best fitting A_2, ϕ_2, A_1, and ϕ_1 parameters of Eq. (1) where A_2 is the amplitude of the twofold intensity modulation, ϕ_2 is the peak angle of that twofold modulation (defined in the range of 0 to 180°), A_1 is the amplitude of the onefold intensity modulation, and ϕ_1 is the angular shift of that onefold modulation (defined in the range of 0 to 360°). B is not shown as it is just the offset of the base level of the FOLZ from zero, which is mainly a function of specimen thickness/density and is rather similar in form to the HAADF image.

The first overarching point is that all these parameter maps are very consistent and show clear repeating patterns across each unit cell, which do not simply mirror the HAADF intensity and clearly contain information absent from the projection-only HAADF image. Almost all prior atomic-resolution imaging techniques in scanning transmission electron microscopy have shown features that are either related directly to the projected potential (annular dark field [31,32], bright field [8], annular bright field [33], ptychography [34,35], and iDPC imaging [36]) or the derivative of the projected potential (atomic resolution differential phase contrast [17] and first moment or center-of-mass imaging [37,38]). The only recent departure from this in atomic-resolution imaging has been *Symmetry-STEM* (S-STEM), in which 4DSTEM diffraction patterns are assessed by applying a symmetry element (e.g., a rotation) and cross-correlating with the original and plotting the cross-correlation coefficients as a function of position [39]. In that case, unprecedented detail is seen that is not simply related to projected potentials, and the details have only partially been explored; however, the method has not yet been widely used at atomic resolution. Also, it only uses small diffracted angles in the first-order Laue zone (basically just low-order diffraction spots overlapping with the primary beam). Thus, mapping features related to high-angle electron diffraction to a higher-order Laue zone, whatever the precise interpretation thereof, reveals things never previously seen in atomic resolution STEM imaging. In this work, the details of what is seen in this specific case are described first, prior to investigating what physically meaningful information can be determined from these maps by comparison to theory.

For specific parameters, the A_2 map shows a hitherto unexpected feature where the strength of the twofold oscillation does not peak at the position of the atom columns in the HAADF image but appears elongated either side of the atom column center, and is small elsewhere—with a much wider elongation of ~ 1.3 Å than the projected column distortion of about 0.2 Å. The ϕ_2 map (corrected in angle as clockwise from $[1\bar{1}0]$, assuming the beam direction is [111]) is centered at around 35°, as expected [30]. Nevertheless, this angle twists near the La-O column positions and around the A_2 peaks: to the lower right of each La-O column, it peaks up to about 41 to 42°, and in between the La atom rows, it dips below 35°. The A_1 map of the unidirectional intensity modulation is particularly surprising as it peaks away from the La column centers, toward one of the arms of the A_2-elongated peak. On the other side of the same La-O column, it shows a large dip in intensity. Finally, the peak angle for the unidirectional distortion measured by the ϕ_1 parameter only shows small variations over most of the image, but shows significant variations near the dips in the A_1 parameter (with very large uncertainties because it is poorly defined when the unidirectional modulation is weak).

B. Atomic resolution diffracted intensity shows the atom displacements

To interpret the atomic resolution detail in diffraction pattern fitting, multislice simulations [40,41] were performed for a suitable supercell of the structure, followed by application of the same polar transformation and fitting as used on the experimental data using a $[111]_M$ direction. This is shown in the upper part of Fig. 3, where HAADF intensity, and the A_2, ϕ_2, and A_1 parameters are plotted (with an upsampling of a factor of 2 to make the plots a little smoother for easier interpretation). For ease of comparison with experimental data, a patch of the same experimental dataset as used to make Fig. 2 was processed as before, and the results were then interpolated by a factor of 4 to allow subpixel alignment. Image patches around 121 different La-columns were then superimposed and averaged to make representative supercell images of each parameter. The visual comparison is evident and whilst the simulations have slightly stronger contrast and better spatial resolution, it is clear that the theory and experiment are mostly in good agreement.

For a detailed explanation of the diffraction physical processes behind these patterns, please see the Supplemental Material [25] Sec. S3, but in short, two patterns should be borne in mind. First, the 3D directions of the $\boldsymbol{b}$-axis and the La-atom displacements make the structure factors of reflections on opposing sides of the FOLZ ring unequal in magnitude. Second, electrons impinging on a crystal slightly offset from a heavy atom column tend to be pulled toward the column by Coulomb interactions, and scattering is biased in this direction. These two effects combine to give much of the contrast seen in the maps.

The key practical point here is that a simulation using a refinement of the published bulk structure [24] produces a diffraction dataset that contains very similar features to those seen in the experimental dataset, which suggests that we can use the simulations for which we know the ground-truth as an interpretation key that allows us to determine crystallographic parameters from experimental maps. The first key useful thing to note is that the asymmetric dip and peak in A_1 magnitude to either side of the La-column centers is reproduced in theory for a perfectly aligned beam along the axis. This shows that

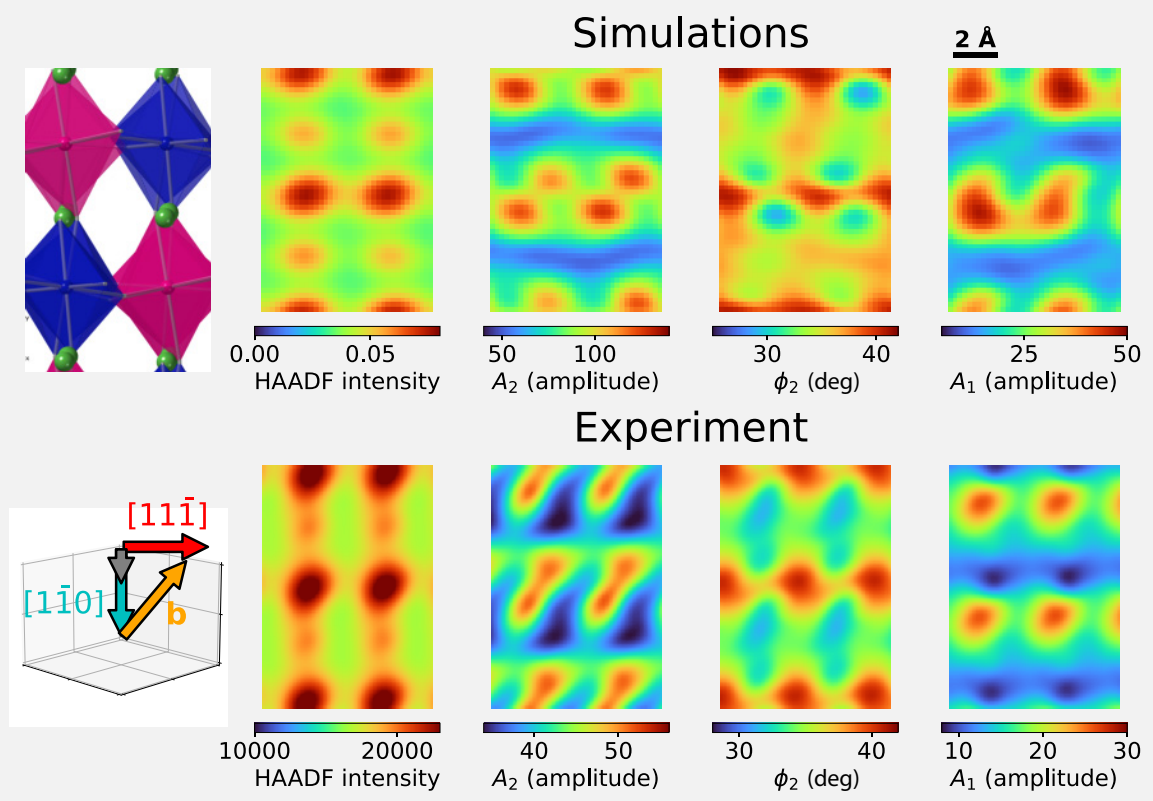


FIG. 3. Comparison of azimuthal fitting applied to a simulated 4DSTEM dataset with a beam direction of $[111]_M$ (after upsampling by a factor of 2) compared to template averaging of experimental fits from the part of the same dataset as shown in Fig. 2 (after upsampling by a factor of 4 before alignment to aid registration with ¼ pixel accuracy). Insets show a schematic diagram of the crystal structure in this projection (atom colors as for Figs. 1 and 2) and a 3D plot of specific crystal directions in this figure (the orange arrow for **b** is pointing up, right, and toward the reader), the gray arrow is the beam direction.

the A_1 parameter is not merely due to mistilt, as we had erroneously assumed in our prior work [30]. It is also clear in this figure that the A_2 parameter map shows dumbbell-like structures peaked to either side of the column center observed in the HAADF image (spacing about 1 3 Å), which are like sharper versions of the streaks or dumbbell-like features in the experimental maps.

The calculation shown is for a $[111]_M$ beam direction (i.e., the direction pointing upward, antiparallel to the direction of electron motion and parallel to the direction of current flow), with the [010] direction pointing to the upper right and up out of the page. This is in the direction from the A_1 peak to the A_1 dip for each La-O column, or alternately from the A_1 peak to the nearby HAADF peak. In view of the correlation between simulation and experiment, and the clear evidence in the Supplemental Material [25] that all this is coming from interaction of the electron beam with the La-atom movements, this then provides an unambiguous method for determining the 3D orientation of the **d**-direction. (The reader is referred to the Supplemental Material [25] Sec. S2 for a demonstration that the same applies to other $\langle 111\rangle_M/\langle 11\bar{1}\rangle_M$-type directions in this crystal structure). It is already known that the intensity of the FOLZ is approximately linearly dependent on the magnitude of atom position modulations along this **d**-direction [19].

Thus, by combining these the HAADF, A_2, ϕ_2, and A_1 maps, we can get the (i) strength of the modulations (from A_2), (ii) the direction of the modulations (and therefore the direction of the **d**-direction with a 180° ambiguity in 3D) (from the ϕ_2 parameter averaged from a few pixels (in this case 3 × 3) around each HAADF peak), and (iii) the absolute sense of the direction in which the **d**-vector is pointing up out of the page (from where the peaks of the A_1 parameter lie with respect to the peak of the HAADF intensity).

C. Mapping atomic displacements in 3D across an interface

From the above, we have determined these parameters from a set of HAADF, A_2, ϕ_2, and A_1 maps. In Fig. 4, this is shown for a 4DSTEM scan across an area containing an interface between an LSAT substrate (top left) and an LCMO thin film. Using the procedure outlined above, Fig. 4 shows arrows (aka a quiver plot), whose angles represent the directions of the **d**-vector for each atomic column, whose heads point in the direction in which the **d**-vector has a positive inclination (i.e., upward from the plane of the page, so an up-right, down-left displacement pattern would give a right-pointing arrow and an up-left, down-right displacement pattern would give a left-pointing arrow), and whose length corresponds to the strength of the atom modulation along this direction. Additionally, the arrows are colored according to the *HSV* color wheel superimposed to represent the 3D direction, where *Hue* represents the azimuthal angle of the **d**-direction about the beam direction, and *Saturation* represents the component of the modulation in-plane (thus paler colors are more vertical),

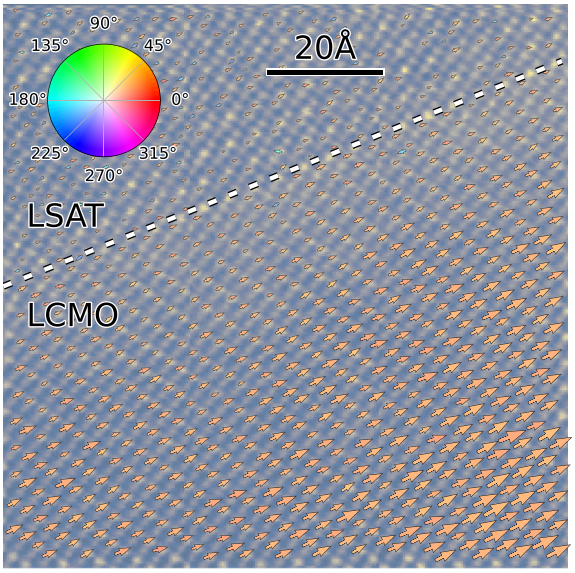


FIG. 4. Atomic resolution imaging of 3D orientations of La atom displacements in a LCMO/LSAT interface area from a 4DSTEM dataset (LSAT substrate above the dotted line, LCMO below). **d** vector orientation and cation displacement are mapped with atomic resolution with arrows: the arrow direction shows the direction in which **d** points out of the page, whereas arrow size shows |**d**|, and color correlates 3D direction in the upper hemisphere according to the color wheel. This is overlaid on a HAADF image calculated from all electrons scattered above 79 mrad to show the correlation with a standard atomic-resolution projection image.

and *Value* is set to 1. In this case, since **b** directions have to be at 30° to the sample plane for any $\langle 111\rangle_M/\langle 11\bar{1}\rangle_M$ direction, so $S = \cos 30° = \sqrt{3}/2$. This map is superimposed on a semitransparent version of the HAADF image as a guide to the eyes. The HAADF image shows the characteristic contrast of LSAT (above the interface) along $\langle 110\rangle_C$ where different patches show slightly different ordering because of internal chemical inhomogeneity. The LCMO (below the interface) shows the typical appearance for a simple perovskite along this beam direction (as also shown in Fig. 2 for the HAADF intensity) with little obvious signs of atomic modulation.

The arrow map shows no clear modulation in the substrate, as expected, with randomly oriented small values (average 2 pm magnitude with an average direction of 58° ± 73° [ACW from horizontal-right]). Throughout the LCMO, however, the modulations all point parallel to the interface toward the top right. The strength of this modulation is very weak for the first few unit cells above the interface (average 4 pm, 25° ± 22° in-plane angle in first 2 nm) but then gradually increases with distance from that interface (average 11 pm, 24° ± 2° in-plane angle > 6 nm from interface). This is in accordance with previous measurements from this very film [11,26], as well as many previous studies showing that strain and properties in thin perovskite films often increase to the full value in a few nm from the substrate, as a result of the constraining effects of the interface [18,19,42,43].

Previous work on LCMO growth concentrated on the effect of using a $\{111\}_C$ growth surface to promote the octahedral

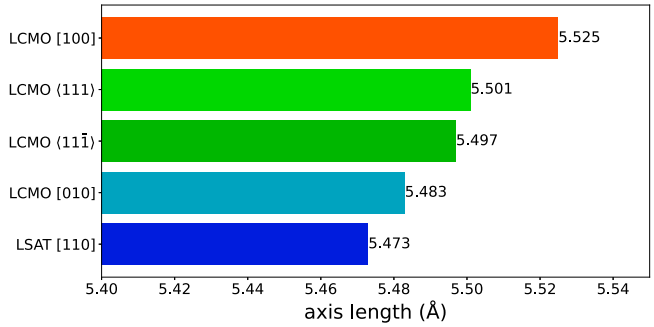


FIG. 5. Axis lengths for different directions in LCMO equivalent to cubic ⟨110⟩ directions, and a comparison to the [110] length in the LSAT substrate.

tilting necessary to create a periodic modulation of B-site size, which then results in ordering of Co and Mn, and thereby strong antiferrimagnetic ordering with a strong magnetic moment [26]. However, the present result indicates that this growth surface promotes in-plane ***b***-axis orientation of the crystal structure, bringing the A-site modulations into the substrate plane. It was speculated in our prior work [26], based on strain considerations, that this might be the case for films on LSAT, but no evidence was presented at the time to confirm or deny this hypothesis. The same trend of the the ***b***-axis lying in plane has been seen in seven atomic-resolution datasets from different areas of the same film. A similar approach has also been applied to a dataset from the film recorded over a much larger image area (not at atomic resolution) and the same still holds true (although absolute mapping of the sense of the ***b***-axis inclination is then not possible because of not having both the atomic resolution imaging of column positions and the A_1 parameter peak positions); this is shown in the Supplemental Material [25] (Fig. S7). As has previously been concluded, octahedral tilting and A-site modulation are all connected in complex oxides like this [19,26]. A key outcome of the present work is that promoting a particular A-site modulation direction appears to be a powerful way to control the octahedral tilting.

IV. DISCUSSION

A. Atomic resolution 3D displacement mapping gives new insights into thin film growth

This brings us to the question of why the A-site modulation should be preferentially in-plane. Generally, domain orientations in perovskite thin films have mainly been found to be determined by strain minimization (for instance, Lebedev *et al.* [44] and MacLaren *et al.* [45]). As it turns out, this may also be true here. This is summarized visually in Fig. 5. LSAT should have a relatively short pseudocubic ⟨110⟩ vector of length 5.473 Å. The ***b***-axis of LCMO should be 5.483 Å in length (so 0.18% compressive strain), $[11\bar{1}]_M/[1\bar{1}\bar{1}]_M$ should be 5.497 Å (0.46% compressive strain), and $[111]_M/[1\bar{1}1]_M$ should be 5.501 Å (0.52% compressive strain). So, all of these could be relatively low strain if lying in-plane. In contrast, the ***a***-axis of LCMO should be 5.525 Å, which is a significantly higher strain of 0.94%. So, the most energetically favorable

configurations will be with **b** and two $\langle 111\rangle_M/\langle 11\bar{1}\rangle_M$ axes in plane on the (111) surface of the LSAT (in other words, a $(101)_M$ film plane [46,47]). This results in a slightly larger spacing normal to the interface (2.25 Å unstrained) than it would for ***a***-axis in-plane (2.24 Å unstrained) (ignoring any Poisson's ratio effects, which would probably increase this further [42]), which probably creates more space to incorporate ordered layers of larger Co atoms. Also, Kjaernes *et al.* [47] reported that $(101)_{Pbnm}$ growth promotes a strong modulation of $(101)_{Pbnm}$ plane spacings, giving alternate larger and smaller plane spacings out-of-plane, which would create larger and smaller spaces for B-site atoms, among other things. This may well be the reason for better Mn/Co ordering on (111) LSAT than growing on (111) $SrTiO_3$ [26] (which has a larger lattice parameter that would probably not favor the same domain orientations). Better Mn/Co ordering gives better ferrimagnetic ordering and a stronger magnetic moment, and thus better properties. This work, therefore, provides a method for understanding the structural origins of these improved properties and imaging in atomic-resolution detail how those growth choices are affecting the structures that give rise to the important functional properties.

One thing that is clear is that this level of detail about domain structures and how they relate to distinct crystallographic axes in characterization techniques was not seen in any characterization techniques used previously. Perhaps with a lot of sample tilting in the TEM goniometer, evidence could be found for some domains with **b**-directions in plane using TEM nanobeam diffraction (this would require getting [010] on-axis, and since this would require tilts of $> 60^\circ$ for some domains, it is not feasible for most domains). It is possible that the differences between ***b***-axis in-plane and ***a***-axis in-plane could be resolved by careful thin-film x-ray diffraction. But, this method of fitting the high-angle electron scattering provides much more straightforward and highly spatially resolved information than any prior method.

B. Wider significance of this work–atomic resolution crystallography using STEM

In the specific case of perovskite oxides with the $GdFeO_3$ structure (to which the double perovskite structure examined in this work is related), such structures involve an orthorhombic unit cell (or monoclinic or triclinic distortion thereof) with a $\sqrt{2}a \times \sqrt{2}a \times 2a$ cell size and a modulation of the A-site atoms along a direction close to the crystallographic ***b***-axis. The HOLZ-STEM method was originally developed on one of these $-LaFeO_3$ [19] on $SrTiO_3$. However, these are fairly commonly used in functional oxide heterostructures.

One frequently used example is $DyScO_3$, especially for perovskite substrates with a relatively large lattice parameter (pseudocubic a = 3.97 Å). However, this has a big difference in the a and b parameters of about 5%, and a large atomic displacement of these La atoms. Clearly, this is going to affect the structure of the interface between it as a substrate and any film grown epitaxially upon it. Boese *et al.* [48] found that $DyScO_3$ grown in a heterostructure with (100) $SrTiO_3$ had either $[110]_{Pnma}$ or $[001]_{Pnma}$ in-plane. This was performed by careful inspection of contrast in high-resolution TEM. Also, using the apparent interface plane in the images, this means that $[1\bar{1}0]_{Pnma}$ is the out-of-plane direction. This was found subsequently to lead to a puckered interface and a reconstruction where every other interface atom column of Dy is much brighter [49] when viewed along $[110]_{Pnma}$. Now this is relevant way beyond just being a structural curiosity, since these $DyScO_3/SrTiO_3$ interfaces show high conductivity under certain circumstances [49,50], and such structural rearrangements at the interface, dependent on 3D crystallography, may well play into such properties. The method shown in the present work provides a far more sensitive and detailed characterization of this 3D crystallography than would have been possible previously, including showing a capability to quantify any change of A-site modulation strength or direction close to the interface.

As another example, $SrRuO_3$ is also a perovskite with the $GdFeO_3$ structure, but it is intriguing as it is a ferromagnetic metal. As such, it has been widely used as an epitaxially lattice-matched contact in oxide heterostructures as well as for the magnetic properties. It can also show fascinating interfacial properties, such as a topological Hall effect in interfaces with $SrIrO_3$ [51] and interesting charge transfer leading to conductivity in the $SrIrO_3$ [52]. However, in those studies, no consideration was given to any effects of orthorhombic crystal orientation, nor was this looked for. However, it can reasonably be expected that the band structure will be directionally dependent and that growth to favor different surfaces could have a significant influence on growth. The method shown in the present work could provide a lot more information about how the atomic modulations and crystal axes behave in practice if such a study were undertaken.

For a third example, growth of $LaFeO_3$ has been shown to be different on different $(111)_C$ surfaces of different orthorhombic perovskite substrates for growth on $(101)_O$ or $(011)_O$ facets [46] (using $DyScO_3$, $NdGaO_3$, and Gd ScO_3). That was important for magnetic properties, since this allowed controllable switching of the magnetic easy axis. Additionally, there are hints in the RHEED data that the crystallographic distortions are reduced close to the interface, possibly similar to the reduced displacements close to the substrate interface in the present work. However, that work contained no microscopy and either $(101)_O$ or $(011)_O$ growth would leave a possibility of domain formation with different ***b***-axis orientations. How these different domains contribute to micromagnetic textures was unexplored. Combining the methods provided in this work with recent advances in Lorentz imaging of magnetic induction [53] would be a promising way forward for understanding substrate/interface control of magnetic properties in a film.

More generally, beyond perovskites, this work shows a way forward for mapping key parameters from 3D crystallography with atomic column resolution. Any feature of a diffraction pattern that varies across a unit cell as a function of radial or azimuthal angle could be extracted by similar approaches to those of fitting data with appropriate mathematical functions, and if applied to 4DSTEM data taken at suitable spatial resolution, could be investigated at the atomic scale. For example, any modulation or chiral displacement of atoms along a column should leave interpretable signals that could be determined and mapped from intensity distributions on a

HOLZ ring. Of course, each case would need validation by simulation to enable the interpretation of the atomic resolution diffraction signals, in a similar way to that in this work. This will be especially powerful in observing the variation of crystallography at the nano- or atomic-scale (i.e., basically inaccessible to traditional bulk diffraction techniques) in the vicinity of internal interfaces and defects in materials and heterostructures. It would also be incredibly powerful at elucidating the details of structure and composition on a column-resolved scale in larger unit cell complex oxides and other complex compounds, where the structure solution from single crystal x-ray or neutron methods is ambiguous and somewhat depends on starting guesses for the occupancy of different sites (e.g., the work of Azough *et al.* [23]).

V. CONCLUSIONS

In summary, we show that it is possible to directly map the azimuthal variation in intensity of a first-order Laue zone ring in electron diffraction of a double perovskite in atomic resolution 4DSTEM imaging. This can be simply parametrized as the amplitudes and peak angles for twofold and onefold trigonometric functions of azimuthal angle. The resulting parameter maps reveal a wealth of atomic resolution detail when applied to imaging of an La_2CoMnO_6 (LCMO) film along a $\langle 111\rangle_{\text{monoclinic}}/\langle 110\rangle_{\text{cubic}}$ direction. With the aid of theoretical simulations, this allows the unambiguous mapping of atomic displacements in three dimensions from a single scan. This showed the expected suppression of displacement close to the substrate interface, but a rapid rise to close to the bulk value in about 6 nm. However, this also showed an insight, specifically that the $\boldsymbol{b}$-axis sits preferentially in the plane of the interface. Further analysis showed that this likely occurred for strain minimisation reasons, but would have been hard to see by techniques available prior to this work (including standard techniques in STEM imaging). More generally, this work demonstrates a new approach to atomic resolution imaging in the electron microscope that is not simply projection imaging, but explicitly works on mapping 3D crystallographic parameters in atomic resolution images from fitting diffraction features in atomic resolution 4DSTEM datasets. It is anticipated that this broad concept will have a major impact on the atomic-scale understanding of materials and nanostructures in the future, especially in systems where the crystallography is all tied to a single crystal orientation of some fundamental lattice, such as epitaxial systems, domain structures, displacive transformations, and order-disorder transitions.

ACKNOWLEDGMENTS

This work would never have been possible without the EPSRC funding of the grant "Fast Pixel Detectors: a paradigm shift in STEM imaging" (Grant No. EP/M009963/1), which started the work that led to this and funded the computer server used in the calculations. We thank Diamond Light Source for access and support in the use of the electron Physical Science Imaging Centre (Instrument E02 and Proposal No. EM16952) that contributed to the results presented here. The films were grown with the support of the European Research Council (ERC) (Advanced Investigator Grant No. ERC-2009-AdG-247276-NOVOX), the EPSRC (Equipment Account Grant No. EP/K035282/1), and the Isaac Newton Trust [Minute 13.38(k)]. I.M. is grateful to Prof. Peter D. Nellist for helpful discussions as part of the EPSRC grant named above and to the late Prof. John C. H. Spence for helpful discussions and encouragement to pursue work on HOLZ in 4DSTEM.

DATA AVAILABILITY

The data that support the findings of this article are openly available [54].

[1] P. E. Batson, N. Dellby, and O. L. Krivanek, Nature (London) **418**, 617 (2002).
[2] M. Haider, S. Uhlemann, E. Schwan, H. Rose, B. Kabius, and K. Urban, Nature (London) **392**, 768 (1998).
[3] P. D. Nellist, M. F. Chisholm, N. Dellby, O. L. Krivanek, M. F. Murfitt, Z. S. Szilagyi, A. R. Lupini, A. Borisevich, W. H. Sides, and S. J. Pennycook, Science **305**, 1741 (2004).
[4] I. MacLaren, and Q. M. Ramasse, Int. Mater. Rev. **59**, 115 (2014).
[5] S. J. Pennycook and M. Varela, J. Electron Microsc. **60**, S213 (2011).
[6] I. MacLaren, and G. Richter, Philos. Mag. **89**, 169 (2009).
[7] I. MacLaren, L. Q. Wang, B. Schaffer, Q. M. Ramasse, A. J. Craven, S. M. Selbach, N. A. Spaldin, S. Miao, K. Kalantari, and I. M. Reaney, Adv. Func. Mater. **23**, 683 (2013).
[8] I. MacLaren, L. Q. Wang, O. Morris, A. J. Craven, R. L. Stamps, B. Schaffer, Q. M. Ramasse, S. Miao, K. Kalantari, I. Sterianou *et al.*, APL Mater. **1**, 021102 (2013).
[9] C.-C. Chen, C. Zhu, E. R. White, C.-Y. Chiu, M. C. Scott, B. C. Regan, L. D. Marks, Y. Huang, and J. Miao, Nature (London) **496**, 74 (2013).
[10] C. Ophus, Microsc. Microanal. **25**, 563 (2019).
[11] I. MacLaren, T. A. Macgregor, C. S. Allen, and A. I. Kirkland, APL Mater. **8**, 110901 (2020).
[12] A. V. Crewe, J. Wall, and J. Langmore, Science **168**, 1338 (1970).
[13] S. J. Pennycook, and D. E. Jesson, Ultramicroscopy **37**, 14 (1991).
[14] S. D. Findlay, N. Shibata, H. Sawada, E. Okunishi, Y. Kondo, and Y. Ikuhara, Ultramicroscopy **110**, 903 (2010).
[15] J. M. LeBeau, A. J. D'Alfonso, S. D. Findlay, S. Stemmer, and L. J. Allen, Phys. Rev. B **80**, 174106 (2009).
[16] J. N. Chapman, I. R. McFadyen, and S. McVitie, IEEE Trans. Magn. **26**, 1506 (1990).
[17] N. Shibata, S. D. Findlay, Y. Kohno, H. Sawada, Y. Kondo, and Y. Ikuhara, Nat. Phys. **8**, 611 (2012).

[18] M. Nord, J. Barthel, C. S. Allen, D. McGrouther, A. I. Kirkland, and I. MacLaren, Ultramicroscopy **226**, 113296 (2021).
[19] M. Nord, A. Ross, D. McGrouther, J. Barthel, M. Moreau, I. Hallsteinsen, T. Tybell, and I. MacLaren, Phys. Rev. Mater. **3**, 063605 (2019).
[20] F. T. Huang, A. Gloter, M. W. Chu, F. C. Chou, G. J. Shu, L. K. Liu, C. H. Chen, and C. Colliex, Phys. Rev. Lett. **105**, 125502 (2010).
[21] D. I. Woodward and I. M. Reaney, Acta Crystallogr. Sect. B-Struct. Commun. **61**, 387 (2005).
[22] A. M. Glazer, Acta Crystallogr. Sect. B-Struct. Commun. B **28**, 3384 (1972).
[23] F. Azough, R. I. Cernik, B. Schaffer, D. Kepaptsoglou, Q. M. Ramasse, M. Bigatti, A. Ali, I. MacLaren, J. Barthel, M. Molinari *et al.*, Inorg. Chem. **55**, 3338 (2016).
[24] C. L. Bull, H. Y. Playford, K. S. Knight, G. B. G. Stenning, and M. G. Tucker, Phys. Rev. B **94**, 014102 (2016).
[25] See Supplemental Material at http://link.aps.org/supplemental/10.1103/p6qm-hpvk for crystallographic proof of the displacement direction, demonstration that the mapping works for different crystallographic directions from simulation, investigations in simulation of the origins of the features in the parameter maps, an investigation of the effects of convergence angle and defocus on the contrast, and a larger area mapping of the direction of atomic displacement.
[26] J. E. Kleibeuker, E.-M. Choi, E. D. Jones, T.-M. Yu, B. Sala, B. A. MacLaren, D. Kepaptsoglou, D. Hernandez-Maldonado, Q. M. Ramasse, L. Jones *et al.*, NPG Asia Materials **9**, e406 (2017).
[27] J. Barthel, Ultramicroscopy **193**, 1 (2018).
[28] B. D. Forbes, A. V. Martin, S. D. Findlay, A. J. D'Alfonso, and L. J. Allen, Phys. Rev. B **82**, 104103 (2010).
[29] M. Nord, P. E. Vullum, I. MacLaren, T. Tybell, and R. Holmestad, Advanced Structural and Chemical Imaging **3**, 9 (2017).
[30] A. Silinga, C. S. Allen, J. Barthel, C. Ophus, and I. MacLaren, Microsc. Microanal. **29**, 1682 (2023).
[31] P. Hartel, H. Rose, and C. Dinges, Ultramicroscopy **63**, 93 (1996).
[32] A. V. Crewe, J. Wall, and L. M. Welter, J. Appl. Phys. **39**, 5861 (1968).
[33] S. D. Findlay, N. Shibata, H. Sawada, E. Okunishi, Y. Kondo, T. Yamamoto, and Y. Ikuhara, Appl. Phys. Lett. **95**, 191913 (2009).
[34] P. D. Nellist and J. M. Rodenburg, Acta Crystallogr. A **54**, 49 (1998).
[35] H. Yang, L. Jones, H. Ryll, M. Simson, H. Soltau, Y. Kondo, R. Sagawa, H. Banba, I. Maclaren, and P. D. Nellist, J. Phys. Conf. Ser. **644**, 012032 (2015).
[36] I. Lazić, E. G. T. Bosch, and S. Lazar, Ultramicroscopy **160**, 265 (2016).
[37] K. Muller, F. F. Krause, A. Beche, M. Schowalter, V. Galioit, S. Loffler, J. Verbeeck, J. Zweck, P. Schattschneider, and A. Rosenauer, Nat. Commun. **5**, 5653 (2014).
[38] W. Gao, C. Addiego, H. Wang, X. Yan, Y. Hou, D. Ji, C. Heikes, Y. Zhang, L. Li, H. Huyan *et al.*, Nature (London) **575**, 480 (2019).
[39] M. Krajnak and J. Etheridge, Proc. Natl. Acad. Sci. USA **117**, 27805 (2020).
[40] P. Goodman and A. F. Moodie, Acta Crystallogr. A **30**, 280 (1974).
[41] J. M. Cowley and A. F. Moodie, Acta Crystallogr. **10**, 609 (1957).
[42] I. MacLaren, Z. L. Wang, H. S. Wang, and Q. Li, Appl. Phys. Lett. **80**, 1406 (2002).
[43] A. Y. Borisevich, H. J. Chang, M. Huijben, M. P. Oxley, S. Okamoto, M. K. Niranjan, J. D. Burton, E. Y. Tsymbal, Y. H. Chu, P. Yu *et al.*, Phys. Rev. Lett. **105**, 087204 (2010).
[44] O. I. Lebedev, J. Verbeeck, G. V. Tendeloo, S. Amelinckx, F. S. Razavi, and H. U. Habermeier, Philos. Mag. A **81**, 2865 (2001).
[45] I. MacLaren, Z. L. Wang, H. S. Wang, and Q. Li, Philos. Mag. A **82**, 1405 (2002).
[46] K. Kjaernes, I. Hallsteinsen, R. V. Chopdekar, M. Moreau, T. Bolstad, I. H. Svenum, S. M. Selbach, and T. Tybell, Phys. Rev. B **103**, 224435 (2021).
[47] K. Kjaernes, T. Bolstad, D. M. Evans, E. Lysne, B. A. D. Williamson, D. Meier, S. M. Selbach, and T. Tybell, arXiv:2011.12874.
[48] M. Boese, T. Heeg, J. Schubert, and M. Luysberg, J. Mater. Sci. **41**, 4434 (2006).
[49] M. Luysberg, M. Heidelmann, L. Houben, M. Boese, T. Heeg, J. Schubert, and M. Roeckerath, Acta Mater. **57**, 3192 (2009).
[50] D. F. Li, Y. Wang, and J. Y. Dai, Appl. Phys. Lett. **98**, 122108 (2011).
[51] J. Matsuno, N. Ogawa, K. Yasuda, F. Kagawa, W. Koshibae, N. Nagaosa, Y. Tokura, and M. Kawasaki, Sci. Adv. **2**, e1600304 (2016).
[52] J. N. Nelson, N. J. Schreiber, A. B. Georgescu, B. H. Goodge, B. D. Faeth, C. T. Parzyck, C. Zeledon, L. F. Kourkoutis, A. J. Millis, A. Georges *et al.*, Sci. Adv. **8**, eabj0481 (2022).
[53] M. Krajnak, D. McGrouther, D. Maneuski, V. O'Shea, and S. McVitie, Ultramicroscopy **165**, 42 (2016).
[54] I. MacLaren, A. Silinga, J. Barthel, J. Kleibeuker, J. L. MacManus-Driscoll, C. S. Allen, and A. I. Kirkland, Atomic resolution imaging of the strength and 3D direction of atomic displacements in functional oxide thin films Enlighten Research Data (2025), https://researchdata.gla.ac.uk/2014/.